Bulk micro-machined wide-band aero-acoustic microphone and its application to acoustic ranging

Bulk micro-machined wide-band aero-acoustic microphone and its application to acoustic ranging

Z J Zhou[1,2]**, L Rufer**[2]**, E Salze**[3]**, P Yuldashev**[3,4]**, S Ollivier**[5] **and M Wong**[1,6]

[1] Department of Electronic and Computer Engineering, The Hong Kong University of Science and Technology, Hong Kong
[2] TIMA Laboratory (CNRS, G-INP, UJF), Grenoble, France
[3] LMFA UMR CNRS 5509, École Centrale de Lyon, Ecully, France
[4] Department of General Physics and Condensed Matter Physics, Faculty of Physics, Lomonosov Moscow State University, Moscow, Russia
[5] LMFA UMR CNRS 5509, Université de Lyon 1, Ecully, France

E-mail: eemwong@ece.ust.hk

Abstract

A wide-band aero-acoustic microphone was realized using a bulk micro-machining process based on the deep reactive-ion etching of silicon. The sensing diaphragm is completely sealed, thus eliminating the loss of low-frequency response resulting from pressure equalization through the release etch-holes present on the diaphragm of a previously reported microphone implemented using a surface-micro-machining process. A dynamic sensitivity of $\sim 0.33\ \mu$V/V/Pa was estimated using an acoustic shockwave ('N-wave') generated using a custom-built high-voltage electrical spark-discharge system. This value is comparable to the effective static sensitivity of $\sim 0.28\ \mu$V/V/Pa measured using a commercial nano-indenter system. The response of the microphone is relatively flat from 6 to 500 kHz, with a resonance frequency of ~ 715 kHz. An array of three microphones was also constructed and tested to demonstrate the application of these microphones to the localization of high frequency and short duration acoustic sources.

(Some figures may appear in colour only in the online journal)

1. Introduction

Advances in aero-acoustic metrology could significantly benefit such industries as high-speed trains, supersonic aviation, space vehicle launches and defense [1–5]. Aero-acoustic experiments can be performed either in outdoor conditions [5], or using scaled models under more tightly-controlled laboratory conditions [4]. Outdoor experiments are often expensive to perform and susceptible to signal contamination by uncontrolled environmental parameters, such as acoustic noise, changes in ambient temperature, humidity and pressure or turbulence. Consequently, laboratory experiments involving scaled models are sometimes preferred by acousticians. Scaled models are also used in preliminary experimental studies of the acoustical response of concert halls or urban areas [6, 7].

When a characteristic feature length is reduced by a scaling factor M, the frequency of an associated acoustic characteristic will be increased by the same factor. Consider the example of a full-scale sniper-localization experiment based on acoustic ranging: the sniper is normally located no more than 250 m [8–11] away from the target and the acoustic bandwidth of interest is ~ 8 kHz for both the muzzle wave and the shockwave [8, 12]. If the test setup is scaled down to 2.5 m, hence $M \sim 100$, then the corresponding bandwidth of interest will be increased by M to ~ 800 kHz.

---

[6] Author to whom any correspondence should be addressed.

In order to obtain high-frequency acoustic waves, acousticians often use electric sparks to generate short duration waves in laboratory experiments. A high-voltage electrical spark-discharge system is known to generate an acoustic excitation covering a wide bandwidth of the order of tens to hundreds of kilohertz [13–15]. A small gap between the electrodes (<8 mm) is used for linear acoustics applications like studying the acoustics of a concert hall [16], and larger gaps (>10 mm) can be used for nonlinear acoustics studies to simulate either a Mach wave or a blast wave since the generated waveform is close to an *N*-wave [17, 18]. While a high-voltage electrical spark-discharge system generates an acoustic excitation over a wide bandwidth up to hundreds of kilohertz, there is presently no microphone calibrated to cover this frequency range for aero-acoustic experiments. Acousticians are mostly limited to 140 kHz when using classical capacitive microphones [19]. The same difficulty arises when measuring weak shockwaves like those generated by focused laser sparks or gunshot noise. Certain optical measurements can also be used, but the estimation of the pressure wave is not straightforward and is limited to special cases, such as strong shocks, high pressure levels, plane or spherical waves [15, 20].

The requirements concerning the frequency range can be met using micro-fabricated microphones. Moreover, the small dimensions of such microphones potentially enable the realization of a dense microphone-array and provide a metrology sensor for studying turbulent flows with high spatial resolution. Different sensing mechanisms, such as capacitive [21], piezoelectric [22], optical [23] and piezoresistive [24] have been applied to realize high-frequency aero-acoustic micro-fabricated microphones. Each has its own relative merits and demerits. For capacitive microphones [21], high sensitivity to pressure and low sensitivity to temperature can be obtained, but the performance could be degraded by parasitic capacitance and the bandwidth limited by squeezed-film damping [25]. Piezoelectric microphones [22] are traditionally used for higher-frequency acoustic signal generation and detection in air. One of the drawbacks of such a system is the requirement of an 'impedance-matching' layer on the active surface of the transducer to minimize performance degradation resulting from the substantial difference between the acoustic impedance of the transducer and that of the propagation medium. These matching layers are often difficult to integrate using micro-fabrication techniques and their efficacies are typically frequency-dependent. Although piezoelectric transducers can be designed to work in the range of several hundreds of kilohertz, they often operate within a narrow frequency band (due to their resonant behavior) and the sensitivity is relatively low. Optical microphones [23] offer a better immunity to electromagnetic interference and their sensitivity is normally higher than that of the microphones based on other sensing mechanisms. However, the assembly process of aligning an optical fiber to a sensing diaphragm is complicated and limits further dimensional scaling of such microphones. Finally, yet importantly, piezoresistive microphones [24] are relatively easy to fabricate using a complimentary metal–oxide–semiconductor (CMOS)-compatible process. Small diaphragm sizes can be readily

Table 1. Material properties of the LS-SiN diaphragm.

Density (kg m^{-3})	3000
Young's modulus (GPa)	207
Poisson's ratio (-)	0.27
Residual stress (MPa)	165

realized to offer resonance frequencies above several hundreds of kilohertz, thus allowing wide bandwidths and a good spatial resolution. The main drawbacks are a relatively higher sensitivity to temperature variation and higher noise level [26, 27] associated with the piezoresistors.

Hitherto constrained by inadequate pressure measurement techniques, all previously demonstrated devices have rarely been calibrated to frequencies beyond 150 kHz [19, 21]. In order to permit acoustical studies of waves with frequencies in the range from ∼10 to ∼500 kHz or more, and pressure level in the range from 10 to 2000 Pa or more, a surface-micro-machined piezoresistive microphone with a resonance frequency of ∼400 kHz has been fabricated and reported [28]. However, due to the need to incorporate release etch-holes on the sensing diaphragm, an 'acoustic short-circuit' was formed and the characteristics of the device were compromised at frequencies below ∼100 kHz. In practice, these etch-holes could be sealed using chemical vapor deposited materials, such as the one based on a parylene-sealing technique [29]. But these techniques greatly complicate the fabrication process.

In this paper the design, fabrication, calibration and application of a new piezoresistive microphone constructed using a simple bulk micro-machining process based on the deep reactive-ion etching (DRIE) of silicon (Si) are described. The sensing diaphragm is released from its 'back side' [22], thus eliminating the need to incorporate release etch-holes and resulting in devices demonstrating significantly improved low-frequency characteristics. The design and the fabrication of the microphone are first described. The electrical, mechanical and acoustical characteristics of the microphone are next reported. The acoustic frequency response of the new device is compared to that of the one [28] constructed using a surface-micro-machining process. Finally, a three-microphone array was constructed to demonstrate the utility of these high-frequency microphones in localizing a high frequency and short duration sound source.

2. Device design

A classical structure with four sensing piezoresistors placed in the middle of each side of a fully clamped square 'sensing' diaphragm is adopted in the present design. Reference resistors are also placed on the rigid substrate adjacent to each piezoresistor. These sensing and reference resistors are connected to form a Wheatstone bridge, as shown in figure 1. The diaphragm is fabricated using low-stress Si nitride (LS-SiN), the relevant material properties of which are summarized in table 1 [28]. The slight tension in the LS-SiN material not only prevents the diaphragm from buckling but also increases the effective spring constant of the sensing diaphragm, hence also the bandwidth.
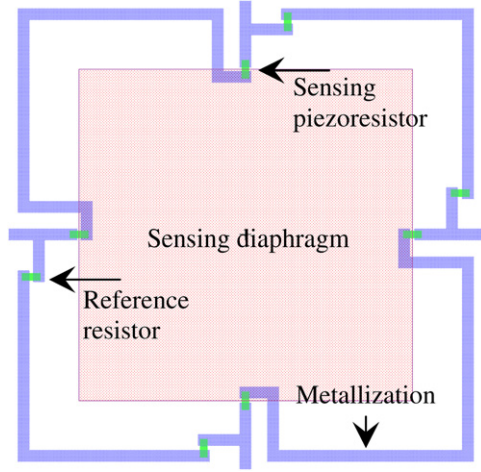
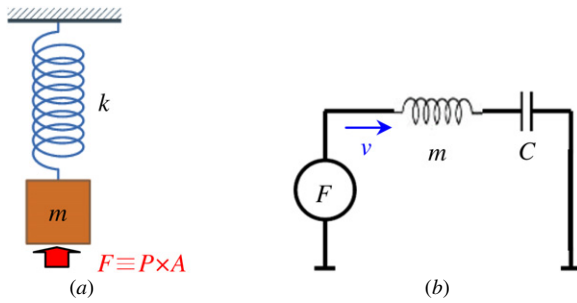**Figure 1.** Schematic layout of a fully clamped square diaphragm.

Figure 2. (*a*) A schematic mechanical model and (*b*) the analogous electrical model of the microphone.

The mechanical behavior of the diaphragm can be approximately modeled using a single degree-of-freedom lumped spring-mass system, leading to a resonance frequency f_r given by

$$f_r = \frac{1}{2\pi}\sqrt{\frac{k}{m}}, \qquad (1)$$

where k is the effective spring constant and m is the effective mass. With $f_r \sim 840$ kHz and $m \sim 3.95 \times 10^{-11}$ kg deduced

using a finite-element simulator (ANSYS), one calculates an approximate value of 1100 N m^{-1} for k.

The mechanical transfer function H (mechanical sensitivity) of the microphone is defined in equation (2):

$$H = \frac{\text{Displacement}}{\text{Pressure}} = \frac{\int v\, dt}{P} = \frac{A\int v\, dt}{F} = A\int \frac{1}{Z_m}\, dt, \quad (2)$$

where v is the diaphragm volume velocity; t is time; P is the pressure applied on the diaphragm; A is the diaphragm area; $F \equiv P \times A$ is the equivalent applied force and Z_m, a measure of how much the diaphragm resists motion when acted upon by F, is the mechanical impedance of the diaphragm. The Fourier transform of equation (2) is

$$H(j\omega) = A\frac{1}{j\omega}\frac{1}{Z_m} = A\frac{1}{j\omega}\frac{1}{\frac{1}{j\omega C} + j\omega m}, \quad (3)$$

where ω is the angular frequency and $C \equiv 1/k$ is the effective mechanical compliance. The mechanical and acoustical representation of the microphone is shown in figure 2(*a*). The corresponding electric circuit shown in figure 2(*b*) can be analyzed using conventional numerical circuit simulators. The simulated frequency-response of the microphone using the parameters listed in table 1 is shown in figure 3.

3. Device fabrication

The fabrication started with the formation of a composite etch-stop layer consisting of a 0.1 μm thick amorphous Si (a-Si) deposited on a 0.5 μm thick oxide thermally grown on a 300 μm thick, (1 0 0)-oriented double-side polished *p*-type Si wafer. This was followed by a sequential deposition of a 0.4 μm thick first LS-SiN layer and a 0.6 μm thick a-Si layer (figure 4(*a*)). The a-Si layer on the back side of the wafer was removed before that on the front side was crystallized using a metal-induced lateral crystallization (MILC) technique [30] at 590 °C for 24 h. The resulting MILC polycrystalline Si (poly-Si) was patterned before being doubly implanted with boron (B). The dose of each implantation was 2.1×10^{14} cm^{-2}; the energies were 45 and 150 keV. Consequently, the total dose was 4.2×10^{14} cm^{-2} and the effective doping concentration was 7×10^{18} cm^{-3}. The implanted B was subsequently
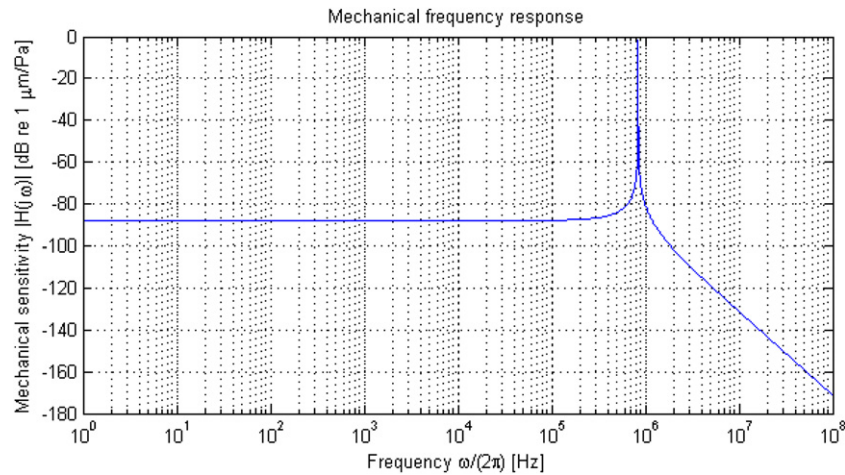

Figure 3. Calculated mechanical frequency response of the microphone.

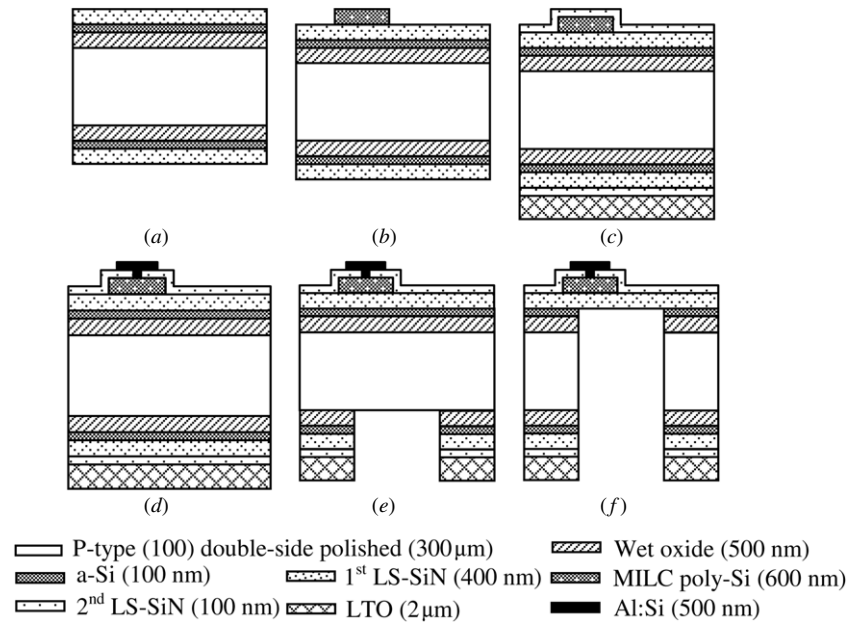|	
▭ P-type (100) double-side polished (300 μm)	▨ Wet oxide (500 nm)
▤ a-Si (100 nm) ⬚ 1st LS-SiN (400 nm)	▨ MILC poly-Si (600 nm)
▭ 2nd LS-SiN (100 nm) ▨ LTO (2 μm)	■ Al:Si (500 nm)

Figure 4. Evolution of the schematic device cross-sections throughout the fabrication process.

activated at 1000 °C for 1.5 h in nitrogen (figure 4(*b*)). After the deposition of a second 0.1 μm thick LS-SiN layer to complete the construction of the sensing diaphragm, a 2 μm thick low-temperature oxide (LTO) was formed on the back side of the wafer as an etch-mask for the subsequent DRIE of Si (figure 4(*c*)). Contact holes to the poly-Si were then opened through the second LS-SiN and heavily implanted with 40 keV B at a dose of 6×10^{15} cm^{-2}. Following dopant-activation at 900 °C for 30 min, a 0.5 μm thick aluminum:Si alloy (Al:Si) was deposited and patterned to form the interconnections (figure 4(*d*)). Contact sintering was done in forming gas at 400 °C for 30 min.

The diaphragm release process started with the coating and patterning of a 3 μm thick photoresist on the stack of thin films on the back side of the wafer. The stack, consisting of LTO, LS-SiN, a-Si and thermal oxide, was etched to reveal the bulk of the Si substrate (figure 4(*e*)). DRIE was used to etch through the Si substrate, stopping only upon reaching the thermal oxide layer on the other side of the wafer. This oxide was subsequently dry etched, stopping at its interface with the crystallized first a-Si layer. Finally the diaphragm was released (figure 4(*f*)) by etching away the crystallized first a-Si layer in an inductively coupled HBr plasma, with a Si:LS-SiN etch selectivity of ∼4:1. Shown in figure 5(*a*) is a planview photograph of the front-side of a microphone after the release of the diaphragm and in figure 5(*b*) a corresponding cross-sectional secondary electron micrograph. The various resistors and the interconnections are clearly visible in figure 5(*a*).

In addition to defining the diaphragm area during the 'back-side photolithography', narrow 10 μm wide 'scribe' lines surrounding each die were also patterned (figure 6(*a*)). The etch rate in these lines was lower, due to the DRIE lag effect [31, 32], than that in a much larger diaphragm area. Consequently, there was ∼120 μm of Si left at the bottom of these scribe lines, which broadened to ∼25 μm, at the end of
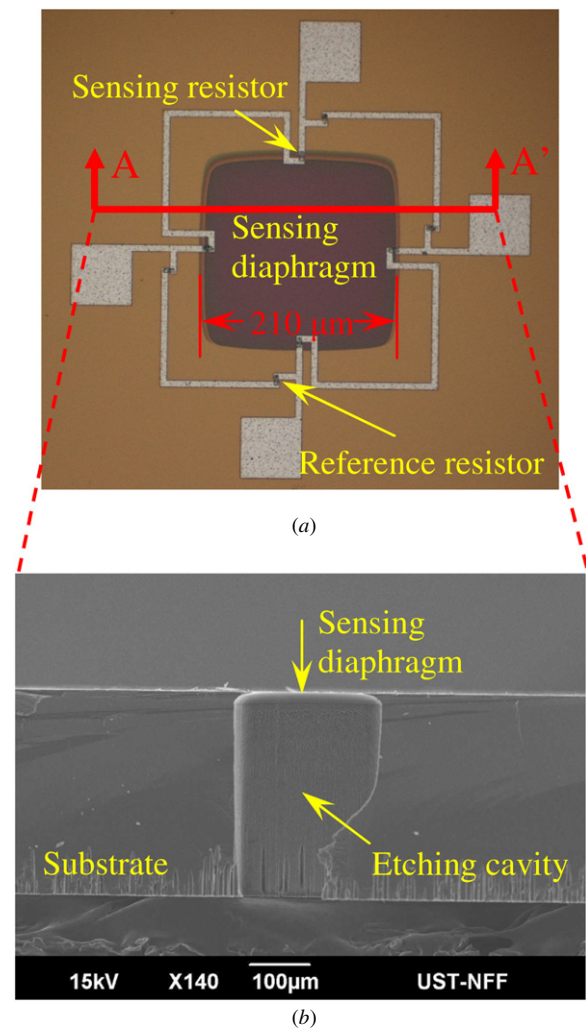

Figure 5. (*a*) Planview photograph of a fabricated microphone and (*b*) cross-sectional secondary electron micrograph cut along AA'.

(a)

120 μm un-etched Si layer
along the scribe line BB'

120μm

180 μm etched Si layer
within the scribe line
along BB'
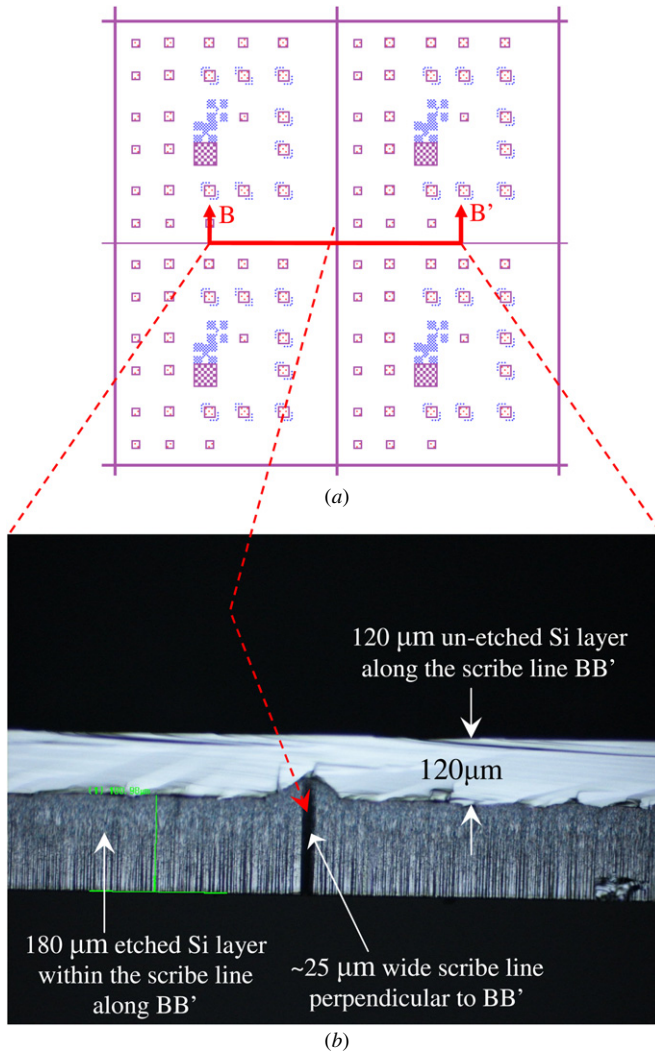
~25 μm wide scribe line
perpendicular to BB'

(b)

Figure 6. (*a*) Schematic layout of four neighboring dies separated by scribe lines and (*b*) cross-sectional view photograph cut along BB' of a scribe line.

the DRIE etch and diaphragm release process (figure 6(*b*)). This thickness of Si provided sufficient mechanical rigidity for regular wafer handling, but weak enough for easy die separation when lightly tapped with a diamond scriber.

4. Device characterization

The electrical properties of the fabricated microphones were then characterized. Any contact resistance between the metallization system and the piezoresistors reduces sensitivity and should be made as small as possible. The sheet resistance R_s of the piezoresistors was measured using a Greek-cross structure. At an estimated doping concentration of 7×10^{18} cm^{-3}, an R_s of ~446.4 Ω was obtained. The contact resistance R_c between the Al:Si interconnect and the heavily doped MILC poly-Si was measured using a Kelvin structure. An R_c of ~37 Ω was obtained, implying a reasonable specific contact resistivity of ~2.3 μΩcm^2. At less than 10% of the R_s of the piezoresistor, this R_c can be considered small.

The die containing the device-under-test (DUT) was attached and wire-bonded onto a printed-circuit board (PCB). The latter was then glued to a metallic holder and fixed on a vibration-free stage. No attempt was made to completely seal the interface between the die and the PCB. Hence the DRIE-etched 'back' chamber remained under ambient pressure. A computer-controlled tribo-indenter (Hysitron® TI900 TriboIndentor) with 25 μm radius conical probe tip was used to apply a point-load near the center of the sensing diaphragm. A Wheatstone bridge, consisting of two sensing and two reference resistors placed respectively on and off the diaphragm, was used to measure the static response of the diaphragm. The output voltage was measured and recorded using an HP 4155 Semiconductor Parameter Analyzer. An equivalent pressure was computed by dividing the force-load by the area of the diaphragm. With a dc bias of 3 V, a linear pressure response (figure 7) from ~0.45 to ~3.6 kPa was obtained, and an effective static sensitivity of ~0.28 μV/V/Pa was deduced.

The dynamic response was characterized with acoustic 'N-waves' generated using a custom-built high-voltage electrical spark-discharge system (figure 8) with a spark-gap of ~13 mm. The DUT was connected to an amplifier with a gain of ~60 dB. Housed in a metallic box, the amplifier was shielded to reduce the electromagnetic interference from the spark source. Based on the previous characterization of spark sources [33], the peak pressure value is found to be ~1.68 kPa at a distance of 10 cm from the source.
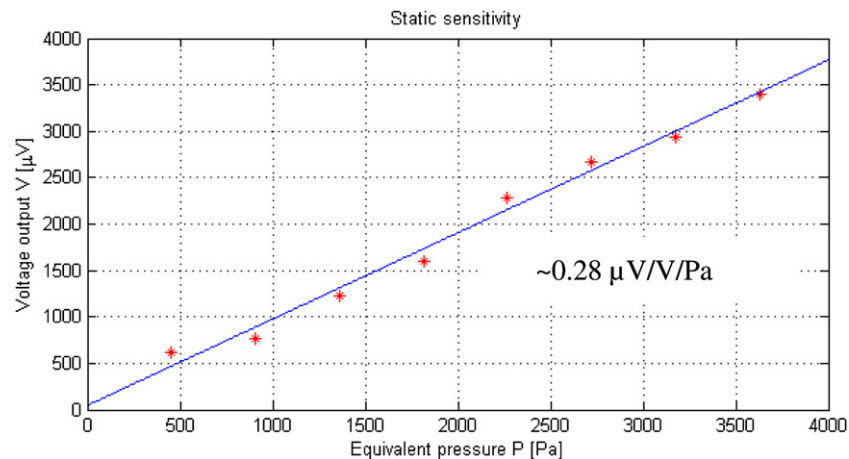

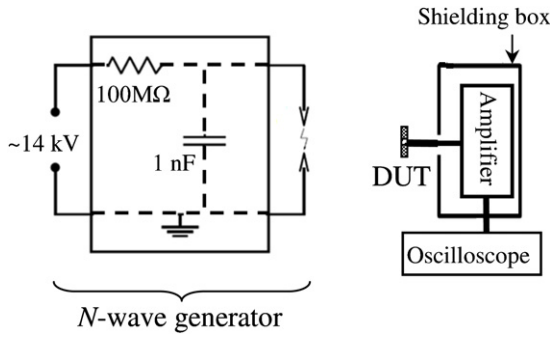**Figure 7.** Static response measured using a nano-indenter system.

Figure 8. Circuit schematic of an electric spark-discharge *N*-wave generator and the DUT.

Compared in figure 9 are the pressure waveform (red) of an 'N-wave' measured using a Schlieren optical technique [20], and the respective voltage waveforms of microphones with acoustically 'leaky' (blue) [28] and 'sealed' (green) diaphragms. It can be seen that both the front- and rear-shocks, as well as the transition between them, were well captured by the new microphone with a 'sealed' diaphragm. On the other hand, the transition, which reflects the low-frequency characteristics of the *N*-wave, was not captured by the 'leaky' microphone.

The single-sided spectra (figure 10) of the measured signals from the microphone and from the optical method were obtained by applying Fourier transform to the time-domain signals in figure 9. The frequency response S (electro-acoustical sensitivity) is defined in equation (4). When using a logarithmic scale in decibels (referring to 1 mV Pa^{-1}), the frequency response can be calculated by directly subtracting the *N*-wave curve (red) from the microphone output waveforms (green/blue) in figure 10:

$$S = \frac{\text{Voltage output}}{\text{Input pressure}} \ (\text{mV/Pa}). \qquad (4)$$

Using the optically calibrated acoustic pressure values, the sensitivities of the microphones were calculated and compared in figure 11. While the low-frequency response of the 'leaky' microphone is strongly attenuated, the newly developed microphone has a relatively flat response from ~6 to ~500 kHz, a dynamic sensitivity of ~0.33 μV/V/Pa and a first-mode f_r of ~715 kHz. The measured f_r is close to but ~15% lower than the value estimated using the lumped-element model. The difference is possibly due to variations in the material properties of the LS-SiN. The resonance of the microphone leads to a strong oscillation superimposed on the captured '*N*-wave' signal. Such oscillation could be damped
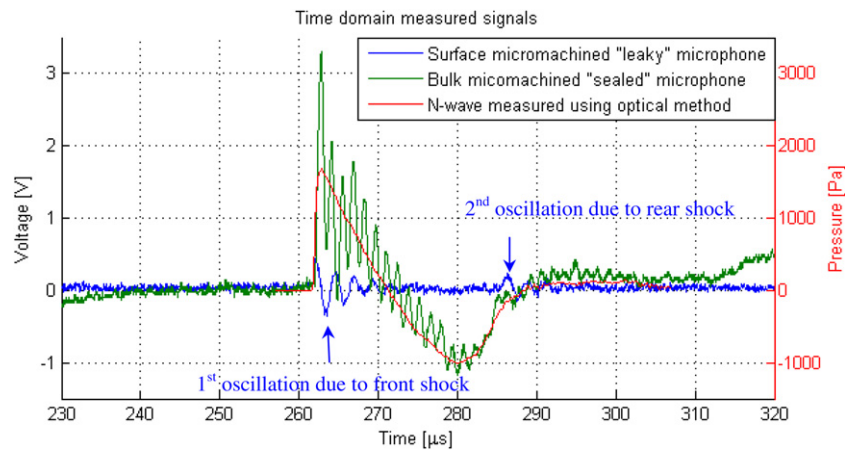

Figure 9. Time–domain waveforms of the optically measured *N*-wave and the electrical response of the microphones with 'leaky' and 'sealed' diaphragms at a microphone to spark-source separation of 10 cm.
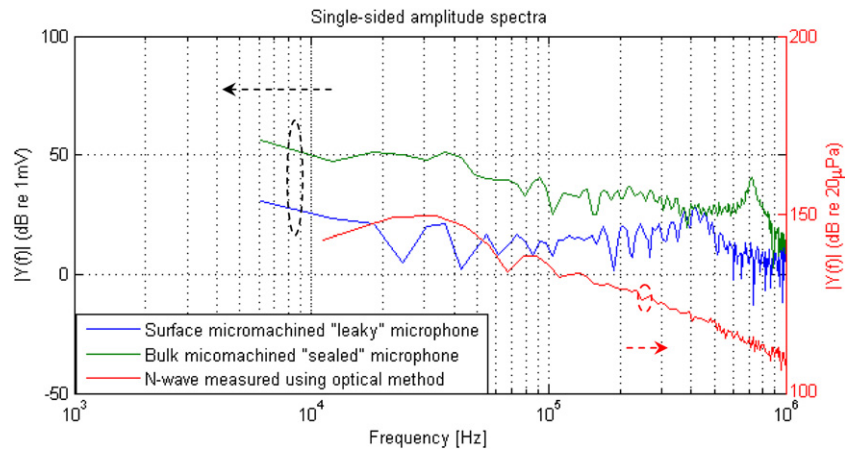

Figure 10. Fourier transforms of the time-domain waveforms in figure 9.
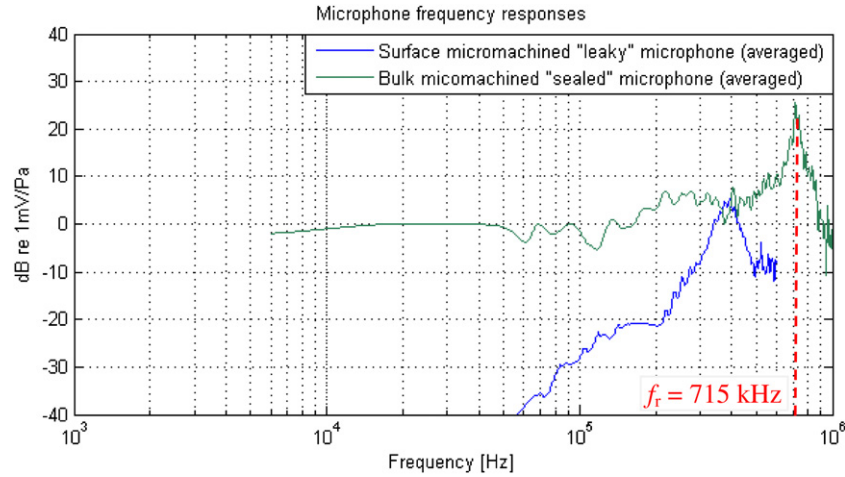
Figure 11. Sensitivities of the microphones with 'leaky' and 'sealed' diaphragms at 3 V dc bias with an amplifier gain of 60 dB.

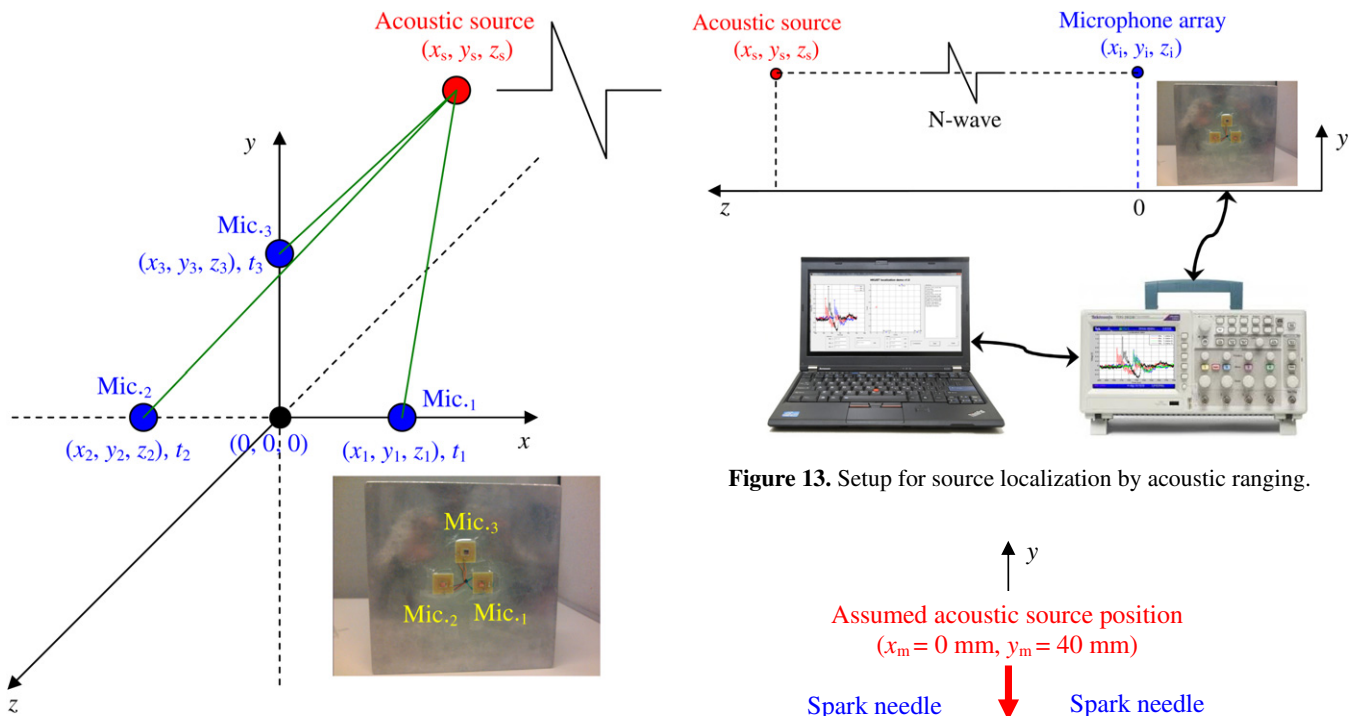**Figure 12.** Cartesian coordinate system for acoustic ranging.

by introducing a properly designed damping mechanism into the microphone structure.

5. Acoustic ranging using an array of three microphones

A prototype setup involving three microphones was constructed to demonstrate the application of these microphones to acoustic ranging (figure 12). The microphones were used to localize the origin of an acoustic 'N-wave', generated using the same electrical spark-discharge system shown in figure 8.

　　Denoting with Cartesian coordinates (x_s, y_s, z_s) the location of a 'spark' event and (x_i, y_i, z_i) the location (table 2) of

Figure 13. Setup for source localization by acoustic ranging.

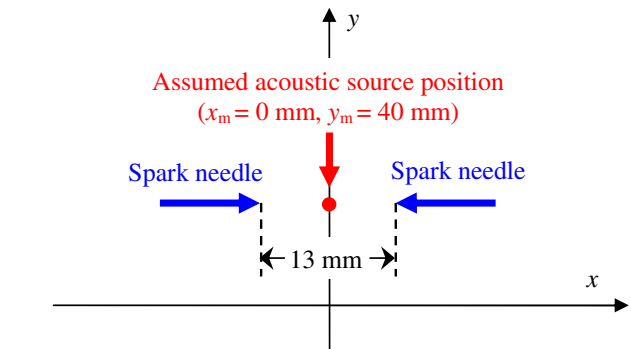**Figure 14.** Schematic diagram showing the definition of (x_m, y_m, z_m).

Table 2. Microphone coordinates (unit: mm).

Microphone i	Coordinates (x_i, y_i, z_i)
$i = 1$	$(25, 0, 0)$
$i = 2$	$(-25, 0, 0)$
$i = 3$	$(0, 40, 0)$

microphone $i = 1, 2$ or 3 (figure 12), one derives

$$(x_s - x_i)^2 + (y_s - y_i)^2 + (z_s - z_i)^2 = (t_i c)^2, \qquad (5)$$
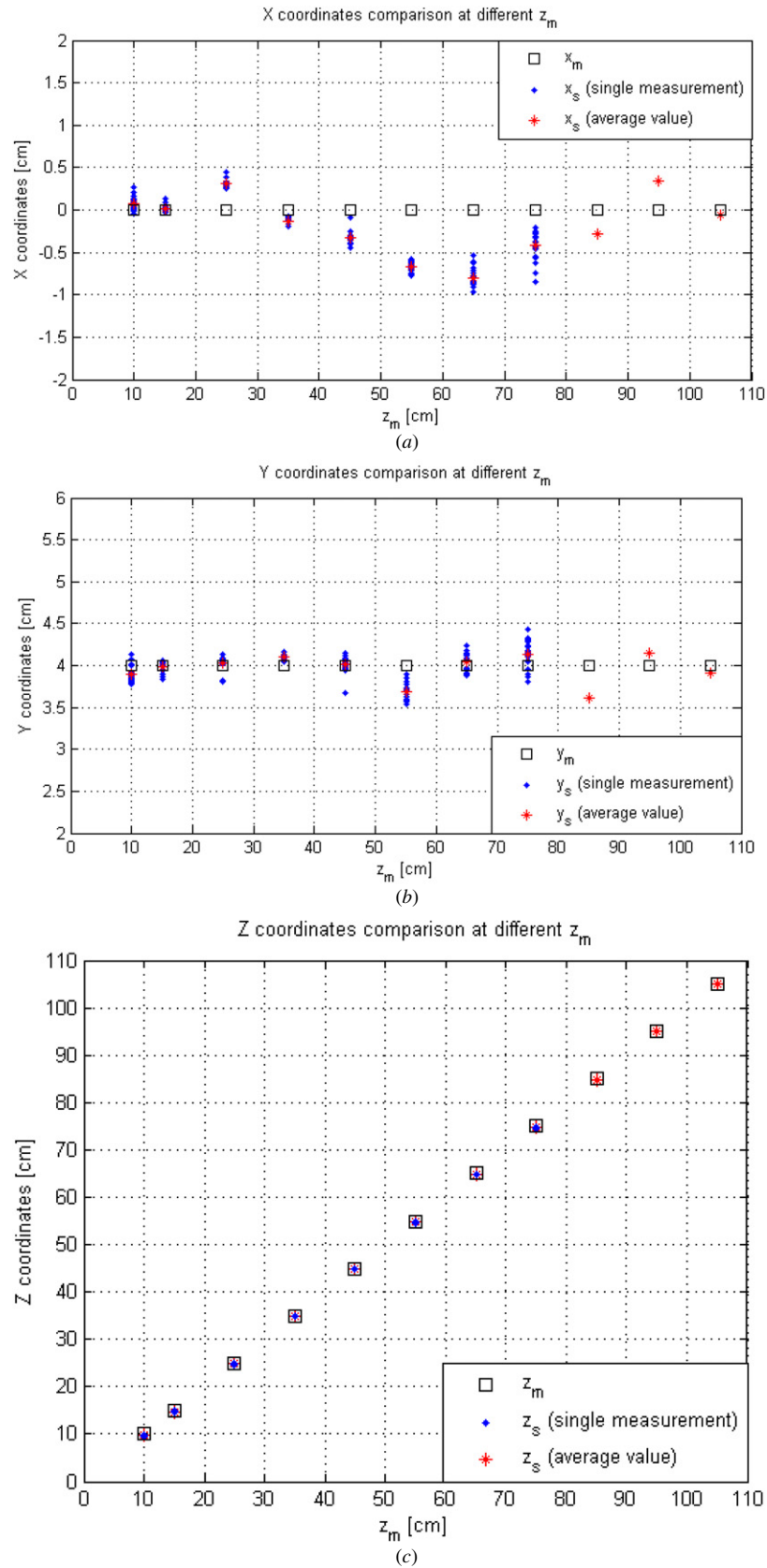
Figure 15. Comparison of the measured (x_m, y_m, z_m) and the calculated (x_s, y_s, z_s), (*a*): x_s versus z_m; (*b*): y_s versus z_m and (*c*): z_s versus z_m. Only ($\overline{x_s}$, $\overline{y_s}$, $\overline{z_s}$) are shown for measurements beyond $z_m = 85$ cm because the corresponding (σ_{x_s}, σ_{y_s}, σ_{z_s}) are large due to severe acoustic attenuation.

Table 3. Acoustic ranging data (unit: mm).

z_m	$\overline{x}_s$	σ_{x_s}	$\overline{y}_s$	σ_{y_s}	$\overline{z}_s$	σ_{z_s}
100	0.8	0.8	38.9	1.0	97.5	0.7
150	0.2	0.4	39.9	0.8	147.5	0.5
250	3.1	0.4	40.3	0.8	247.9	0.8
350	-1.3	0.4	41.0	0.3	348.4	0.3
450	-3.3	0.7	40.2	1.0	448.2	0.3
550	-6.8	0.7	36.8	1.0	547.9	0.6
650	-8.0	1.2	40.5	1.0	648.0	0.2
750	-4.2	1.7	41.4	1.7	747.4	0.9
850	-2.8	–	36.1	–	848.6	–
950	3.4	–	41.6	–	948.9	–
1050	-0.6	–	39.0	–	1049.6	–

where t_i is the transit time of an N-wave from (x_s, y_s, z_s) to (x_i, y_i, z_i) and $c \approx 344.2$ m s^{-1} is the calibrated sound velocity.

The spark generator emits an acoustic 'N-wave', which is accompanied by an electromagnetic pulse. The electrical response of the microphones to both the electromagnetic pulse and the acoustic shock were captured using a Tektronix TDS 2024C oscilloscope. Through a USB cable and using the MATLAB Instrument Control Toolbox based on the National Instruments Virtual Instrument Software Architecture (NI-VISA) standard, the data were transferred to a computer for further analysis (figure 13). Since it is safe to assume the electromagnetic pulse arrived almost 'instantaneously' at the microphones, t_i could be accurately estimated by the time-delay (τ_i) between the response to the electromagnetic pulse and that to the acoustic shock. Consequently

$$(x_s - x_i)^2 + (y_s - y_i)^2 + (z_s - z_i)^2 \approx (\tau_i c)^2. \qquad (6)$$

The resulting system of three equations for $i = 1, 2$ and 3 was used to obtain (x_s, y_s, z_s).

With (x_m, y_m, z_m) denoting the location of the mid-point between the tips of the pair of the discharge needles (figure 14), z_m was varied from 100 to 1050 mm with x_m and y_m fixed respectively at 0 and 40 mm. For each (x_m, y_m, z_m), the (x_s, y_s, z_s) of 20 spark events were deduced using equation (6) and plotted in figure 15, together with the average $(\overline{x}_s, \overline{y}_s, \overline{z}_s)$ of each group of the 20 spark events. The standard deviation $(\sigma_{x_s}, \sigma_{y_s}, \sigma_{z_s})$ of each group of the 20 (x_s, y_s, z_s) was computed and summarized in table 3, and each can be attributed to the uncertainty associated with the finite bandwidth of the acoustic pulse and the deviation of the location of the spark event from (x_m, y_m, z_m). Note that every component of $(\sigma_{x_s}, \sigma_{y_s}, \sigma_{z_s})$ is smaller than the 13 mm separation between the spark needles. Because of the severe attenuation of the N-wave for $z_m > 750$ mm, there is large fluctuation in the estimation of (x_s, y_s, z_s) due to a significantly reduced signal-to-noise ratio. The corresponding large $(\sigma_{x_s}, \sigma_{y_s}, \sigma_{z_s})$ has not been included in table 3.

The resolution of the acoustic ranging system is limited by how accurately the arrival of the shockwave at a given microphone can be captured. This is ultimately constrained by the rise time of the measured shockwave. This rise time is inversely proportional to the bandwidth of the microphone and in the present case can be simply estimated by the resonance frequency f_r. For $z_m \leqslant 750$ mm, the maximum

standard deviation ($\sigma_{ts} \equiv \sqrt{\sigma_{x_s}^2 + \sigma_{y_s}^2 + \sigma_{z_s}^2}$) of the calculated coordinates x_s, y_s and z_s is ~ 2.57 mm, which is larger than $\lambda_r = c/f_r \sim 0.48$ mm for $f_r \sim 715$ kHz. This difference is attributed to the random fluctuation σ_{ss} of the location (x_s, y_s, z_s) of any given spark event from (x_m, y_m, z_m). Treating λ_r as an estimate of the uncertainty in the measurement of length, $\sigma_{ss} \sim 2.52$ mm can be estimated using

$$\sigma_{ts}^2 = \lambda_r^2 + \sigma_{ss}^2. \qquad (7)$$

6. Conclusion

A bulk micro-machining process based on the DRIE of silicon was developed and successfully applied to the fabrication of a wide-band aero-acoustic microphone dedicated to high-frequency measurements. The fabricated microphone was calibrated statically and dynamically, manifesting a relatively linear static pressure response from 0.45 to 3.6 kPa with an effective sensitivity of ~ 0.28 μV/V/Pa and a flat frequency response from 6 to 500 kHz with a dynamic sensitivity of ~ 0.33 μV/V/Pa. The use of these microphones for acoustic ranging was demonstrated using a three-microphone array. The resolution was fine enough to resolve even the random fluctuation (~ 2.52 mm) of the location of a spark event, for a source located within a distance of 750 mm from the microphone array.

References

[1] Schetz J A 2001 Aerodynamics of high-speed trains *Annu. Rev. Fluid Mech.* **33** 371–414
[2] Raghunathan R S, Kim H -D and Setoguchi T 2002 Aerodynamics of high-speed railway train *Prog. Aerosp. Sci.* **38** 469–514
[3] Oerlemans S, Broersma L and Sijtsma P 2007 Quantification of airframe noise using microphone arrays in open and closed wind tunnels *National Aerospace Laboratory NLR, Report*
[4] Remillieux M 2007 Aeroacoustic study of a model-scale landing gear in a semi-anechoic wind-tunnel *MSc Thesis* Virginia Polytechnic Institute and State University
[5] McInerny S A and Olcmen S M 2005 High-intensity rocket noise: nonlinear propagation, atmospheric absorption, and characterization *J. Acoust. Soc. Am.* **117** 578–91
[6] Bolanos J G, Pulkki V, Karppinen P and Haeggstrom E 2013 An optoacoustic point source for acoustic scale model measurements *J. Acoust. Soc. Am.* **133** EL221–7
[7] Picaut J and Simon L 2001 A scale model experiment for the study of sound propagation in urban areas *Appl. Acoust.* **62** 327–40
[8] Duckworth G L, Gilbert D C and Barger J E 1997 Acoustic counter-sniper system *Proc. SPIE* **2938** 262–75

[9] Damarla T, Whipps G and Kaplan L 2008 Sniper localization for asynchronous sensors *Proc. Army Sci. Conf. (Orlando, FL)* (www.dtic.mil/cgi-bin/GetTRDoc?AD= ADA503400&Location=U2&doc=GetTRDoc.pdf)

[10] Damarla T, Kaplan L M and Whipps G T 2010 Sniper localization using acoustic asynchronous sensors *Sensors J. IEEE* **10** 1469–78

[11] Stoughton R 1997 Measurements of small-caliber ballistic shock waves in air *J. Acoust. Soc. Am.* **102** 781–7

[12] Duckworth G L, Barger J E, Carlson S H, Gilbert D C, Knack M L, Korn J and Mullen R J 1999 Fixed and wearable acoustic counter-sniper systems for law enforcement *Proc. SPIE* **3577** 210–30

[13] Wright W M 1983 Propagation in air of *N* waves produced by sparks *J. Acoust. Soc. Am.* **73** 1948–55

[14] Yuldashev P V, Averiyanov M V, Khokhlova V A, Ollivier S and Blanc-Benon P 2008 Nonlinear spherically divergent shock waves propagating in a relaxing medium *Acoust. Phys.* **54** 32–41

[15] Yuldashev P, Ollivier S, Averiyanov M, Sapozhnikov O, Khokhlova V and Blanc-Benon P 2010 Nonlinear propagation of spark-generated *N*-waves in air: modeling and measurements using acoustical and optical methods *J. Acoust. Soc. Am.* **128** 3321–33

[16] Hak C C J M and Bijsterbosch K B A 2009 Room acoustic scale model measurements using a 'spark train' *NAG/DAGA, Rotterdam* pp 946–8

[17] Lipkens B and Blackstock D T 1998 Model experiment to study sonic boom propagation through turbulence: part II. Effect of turbulence intensity and propagation distance through turbulence *J. Acoust. Soc. Am.* **104** 1301–9

[18] Blanc-Benon P, Averiyanov M V, Ollivier S and Khokhlova V A 2010 Random focusing of nonlinear *N*-waves in fully developed turbulence: laboratory scale experiment and theoretical analysis *J. Acoust. Soc. Am.* **127** 1883

[19] Brüel & Kjær Microphone Type 4138 Manual www.bksv.com/doc/bp2030.pdf

[20] Karzova M, Salze E, Ollivier S, Castelain T, André B, Yuldashev P, Khokhlova V, Sapozhnikov O and Blanc-Benon P 2012 Interaction of weak shocks leading to Mach stem formation in focused beams and reflections from a rigid surface: numerical modeling and experiment *Acoustics 2012 Conf. (Nantes, France)* pp 1117–21

[21] Hansen S T, Ergun A S, Liou W, Auld B A and Khuri-Yakub B T 2004 Wideband micromachined

capacitive microphones with radio frequency detection *J. Acoust. Soc. Am.* **116** 828–42

[22] Williams M D, Griffin B A, Reagan T N, Underbrink J R and Sheplak M 2012 An AlN MEMS piezoelectric microphone for aeroacoustic applications *J. Microelectromech. Syst.* **21** 270–83

[23] Kadirvel K, Taylor R, Horowitz S, Hunt L, Sheplak M and Nishida T 2004 Design and characterization of MEMS optical microphone for aeroacoustic measurement *42nd Aerospace Sciences Meeting and Exhibit (Reno, NV)* pp 1030–9

[24] Sheplak M, Breuer K S and Schmidt M A 1998 A wafer-bonded, silicon-nitride membrane microphone with dielectrically-isolated, single-crystal silicon piezoresistors *Proc. Solid-State Sensor and Actuator Workshop (Cleveland, OH, USA)* pp 23–6

[25] Löfdahl L and Gad-El-Hak M 1999 MEMS-based pressure and shear stress sensors for turbulent flows *Meas. Sci. Technol.* **10** 665

[26] Dieme R, Bosman G, Nishida T and Sheplak M 2006 Sources of excess noise in silicon piezoresistive microphones *J. Acoust. Soc. Am.* **119** 2710–20

[27] Dieme R 2005 Characterization of noise in MEMS piezoresistive microphones *MSc Thesis* University of Florida

[28] Zhou Z J, Rufer L, Wong M, Salze E, Yuldashev P and Ollivier S 2012 Wide-band piezoresistive microphone for aero-acoustic applications *The 11th Annu. IEEE Conf. on Sensors (Taipei, Taiwan, 28–31 Oct.)* pp 818–21

[29] Krause J S, White R D, Moeller M J, Gallman J M, Holup G and De Jong R 2010 MEMS pressure sensor array for aeroacoustic analysis of the turbulent boundary layer *Proc. 48th AIAA Aerospace Sciences* Mtg *(Orlando, FL Jan 4–7)* pp 3555–69

[30] Wang M, Meng Z, Zohar Y and Wong M 2001 Metal-induced laterally crystallized polycrystalline silicon for integrated sensor applications *IEEE Trans. Electron Devices* **48** 794–800

[31] Gottscho R A, Jurgensen C W and Vitkavage D J 1992 Microscopic uniformity in plasma etching *J. Vac. Sci. Technol. B* **10** 2133–47

[32] Jansen H, de Boer M, Wiegerink R, Tas N, Smulders E, Neagu C and Elwenspoek M 1997 RIE lag in high aspect ratio trench etching of silicon *Microelectron. Eng.* **35** 45–50

[33] Ollivier S, Salze E, Averiyanov M, Yuldashev P V, Khokhlova V and Blanc-Benon P 2012 Calibration method for high frequency microphones *Acoustics 2012 Conf. (Nantes, France)* pp 3509–13